remote sensing

MDPI

Article

Influence of Supraglacial Lakes on Accuracy of Inversion of Greenland Ice Sheet Surface Melt Data in Different Passive Microwave Bands

Qian Li [1,2], Che Wang [1,*], Lu An [3,4] and Minghu Ding [2,5]

[1] State Key Laboratory of Urban Environmental Processes and Digital Simulation, Capital Normal University, Beijing 100048, China; 2200902166@cnu.edu.cn
[2] State Key Laboratory of Severe Weather, Chinese Academy of Meteorological Sciences, Beijing 100081, China; dingmh@cma.gov.cn
[3] Center for Spatial Information Science and Sustainable Development Applications, Tongji University, 1239 Siping Road, Shanghai 200092, China; anlu2021@tongji.edu.cn
[4] College of Surveying and Geo-Informatics, Tongji University, 1239 Siping Road, Shanghai 200092, China
[5] Key Laboratory of Polar Atmosphere-Ocean-Ice System for Weather and Climate, Ministry of Education, Shanghai 200438, China
* Correspondence: 6697@cnu.edu.cn

Abstract: The occurrence of Supraglacial Lakes (SGLs) may influence the signals acquired with microwave radiometers, which may result in a degree of uncertainty when employing microwave radiometer data for the detection of surface melt. Accurate monitoring of surface melting requires a reasonable assessment of this uncertainty. However, there is a scarcity of research in this field. Therefore, in this study, we computed surface melt in the vicinity of Automatic Weather Stations (AWSs) by employing Defense Meteorological Satellite Program (DMSP) Ka-band data and Soil Moisture and Ocean Salinity (SMOS) satellite L-band data and extracted SGL pixels by utilizing Sentinel-2 data. A comparison between surface melt results derived from AWS air temperature estimates and those obtained with remote sensing inversion in the two different bands was conducted for sites below the mean snowline elevation during the summers of 2016 to 2020. Compared with sites with no SGLs, the commission error (CO) of DMSP morning and evening data at sites where these water bodies were present increased by 36% and 30%, respectively, and the number of days with CO increased by 12 and 3 days, respectively. The omission error (OM) of SMOS morning and evening data increased by 33% and 32%, respectively, and the number of days with OM increased by 17 and 21 days, respectively. Identifying the source of error is a prerequisite for the improvement of surface melt algorithms, for which this study provides a basis.

Keywords: Greenland Ice Sheet; surface melt; Ka-band; L-band; Supraglacial Lakes

Citation: Li, Q.; Wang, C.; An, L.; Ding, M. Influence of Supraglacial Lakes on Accuracy of Inversion of Greenland Ice Sheet Surface Melt Data in Different Passive Microwave Bands. *Remote Sens.* **2024**, *16*, 1673. https://doi.org/10.3390/rs16101673

Academic Editor: Yi Luo

Received: 3 March 2024
Revised: 3 May 2024
Accepted: 7 May 2024
Published: 9 May 2024

1. Introduction

As the second-largest continental ice sheet after Antarctica, the Greenland Ice Sheet (GrIS) is projected to cause a sea level rise of about 7 m if melted entirely [1]. In recent decades, climate change-induced mass loss from the Greenland Ice Sheet has been the primary driver of sea level rise, contributing approximately 13.7 mm to sea level rise from 1972 to 2018, with the reduction in Surface Mass Balance (SMB) accounting for approximately 34% of the total mass loss [2]. Similarly, from 1992 to 2018, mass loss from the GrIS led to a sea level rise of 10.8 mm, with the decrease in SMB constituting 50.3% of the total mass loss [3]. Projections suggest that mass loss from the GrIS will contribute approximately 4–30 cm to sea level rise by the end of the century [4], with the reduction in SMB being expected to account for around 50% of the mass loss [5]. The decline in SMB is gradually becoming the dominant factor in mass loss from the GrIS. This decline is primarily attributed to the runoff of meltwater from the surface into the ocean [6].

Consequently, investigating the surface melting of the GrIS is paramount to understanding and predicting sea level rise in the context of climate change.

Microwave radiometer data serve as the primary source for determining the surface melting of the GrIS [7]. The passive microwave bands prevalently employed for calculating binary surface melt status (melt or no melt) include the K and Ka bands [8,9]. Nghiem et al. leveraged Defense Meteorological Satellite Program (DMSP) K-band and Ka-band data to monitor the extreme melting range of 98.6% of the GrIS on 12 July 2012 [10]. Colosio et al., by employing Ka-band data, calculated the surface melting of the GrIS spanning the years 1979 to 2019 [8]. The L band is utilized for calculating quantitative surface melt [11,12]. Houtz et al. utilized L-band data from the European Space Agency's (ESA) Soil Moisture and Ocean Salinity (SMOS) satellite to calculate the liquid water content (LWC) of the GrIS from 2011 to 2018 [11]. Mousavi et al. harnessed NASA's Soil Moisture Active Passive (SMAP) satellite L-band data to calculate the melting intensity of the GrIS from 2015 to 2021 [13]. Colliander et al. employed SMAP L-band and AMSR2 (Advanced Microwave Scanning Radiometer-2) K- and Ka-band data together to calculate the LWC of the GrIS [14].

When inverting surface melt data by using Ka and L bands, two key models are involved—MEMLS and LS-MEMLS [9,12]. In the context of surface melting applications, both models postulate the presence of stratified snow on top of glacial ice [9,12]. The MEMLS is capable of simulating frequencies ranging from 5 GHz to 100 GHz, and the number of snow layers can be flexibly chosen [15]. This model was utilized in Tedesco's research study, where it was assumed that the bottom layer consisted of ice, and the total thickness of the snow layer was established at 20 m, with each layer having a fixed thickness of 5 cm [9]. The LS-MEMLS was developed by Schwank et al. [16]. This model builds upon the MEMLS and incorporates modeling components representing multilayer soil beneath the snow cover, aiming to aid in the investigation of soil freeze–thaw conditions or snow cover mapping by applying the L-band data from the SMOS satellite [16]. The LS-MEMLS assumes the presence of a seasonal snow field above glacier ice, which is further divided into wet and dry snow layers [11,12].

In ablation zones, cumulus snow fields exist above glacial ice [17]. At times of less intense melting, the configuration of these two models is consistent with the reality of much of the ablation zones [11,12]. However, at times of more intense melting, the configuration of these two models is oversimplified. During the ablation season (June–August or May–September), snow melting occurs, and surface meltwater forms ice runoff facilitated by topographical features or pools in topographic lows to form SGLs [18–20]. Therefore, for Ka- and L-band data, during the ablation season in ablation zones, there are mixed pixels, such as snow and SGLs, whose existence is inconsistent with the assumptions of the above two models.

The uncertainty that SGLs introduce into the passive microwave inversion of surface melting data has been discussed in previous studies. For example, Houtz et al. stated that L-band data may underestimate the liquid water volume when SGLs are present [11], and Li et al. asserted that the Ka band may cause false-positive retrieval when SGLs are present [21]. However, the uncertainty introduced by SGLs into the inversion of surface melting data in different passive microwave bands has not been confirmed. The accurate monitoring of surface melting necessitates a comprehensive evaluation of this uncertainty. To investigate the impact of SGLs on surface melting data inversion in various passive microwave wavebands, in this study, we primarily conducted the following tasks: DMSP Ka-band and SMOS L-band data were employed to estimate the surface melting of the GrIS from 2011 to 2020, and the spatio-temporal distribution of surface melt and surface melt errors was analyzed (refer to Section 3.1). Subsequently, Sentinel-2 summer data from 2016 to 2020 were utilized to identify SGLs in the vicinity of Automatic Weather Stations (AWSs) (refer to Section 3.2) and examine their influence on Ka-band and L-band data (refer to Section 3.3).

2. Data and Methods

2.1. Data

2.1.1. Passive Microwave Data

In this study, we employed Ka-band (37 GHz) horizontal polarization data, which were obtained with the DMSP-F17 platform's SSMI/S sensor. The projection method employed was EASE-grid 2.0 Northern Hemisphere, Lambert Azimuthal (EPSG: 6931), with a spatial resolution of 25 km [21]. These data are available twice daily, once in the morning and once in the evening. The data obtained by the DMSP satellite in the morning are referred to as DMSP morning data, and those obtained in the evening are referred to as DMSP evening data. Due to the significant variation in melt information captured at different times of the day [22], the melt results of DMSP morning and evening data were calculated separately. Given that horizontal polarization data at 37 GHz are more sensitive to changes in LWC [23], Ka-band horizontal polarization data were chosen for this study. These data can be accessed freely on the EarthData website (https://search.earthdata.nasa.gov/search, accessed on 1 January 2024). In this study, DMSP data from 2011 to 2020 were selected for the calculation of surface melt.

L-band (1.4 GHz) tertiary bright temperature data were obtained with the SMOS satellite at the top of the atmosphere. These data feature two polarization modes, horizontal and vertical, and a total of 14 effective incidence angles, ranging from 2.5° to 62.5° (with a 5° interval, including 40°). The projection method employed was EASE-grid 2.0 Global, Equal-Area (EPSG: 6933), and the spatial resolution was 25 km [24]. These data are available twice daily, once in the morning and once in the afternoon. The data obtained by the SMOS satellite in the morning are hereinafter referred to as SMOS morning data, and those obtained in the afternoon as SMOS evening data. Due to the sampling characteristics of the MIRAS radiometer on the SMOS satellite, data are not provided at all angles of incidence [25]. To eliminate false-positive retrieval, these data require that the number of effective incidence angles provided by the input data be greater than 5 [12]. The data can be accessed freely at the SMOS data center website (https://www.catds.fr/sipad, accessed on 1 January 2024). In this study, SMOS data from 2011 to 2020 were selected for the calculation of surface melt.

In this study, the surface melt results of the GrIS were calculated for the period from 2011 to 2020. The passive microwave data used included DMSP and SMOS morning and evening data. The DMSP satellite data provide the effective number of days, with a value of 365 or 366 days, and the latter has the same parameter but with an average value of 301 days. Figure 1 provides the effective days in Greenland with data for both satellites for the period of 2011 to 2020. It can be seen that the effective days with DMSP satellite data in all regions of Greenland were close to a full year. However, the SMOS satellite data accounted for different effective days in different regions of Greenland (the number of effective days in the north was higher than in the south). This is because the SMOS satellite calculation of the melt status depends on the number of available incidence angles. For a pixel of the SMOS satellite, there are 14 angles of incidence, but not all of them provide brightness temperature. The melt status of a pixel can be calculated when the number of incidence angles providing brightness temperature is greater than 5.

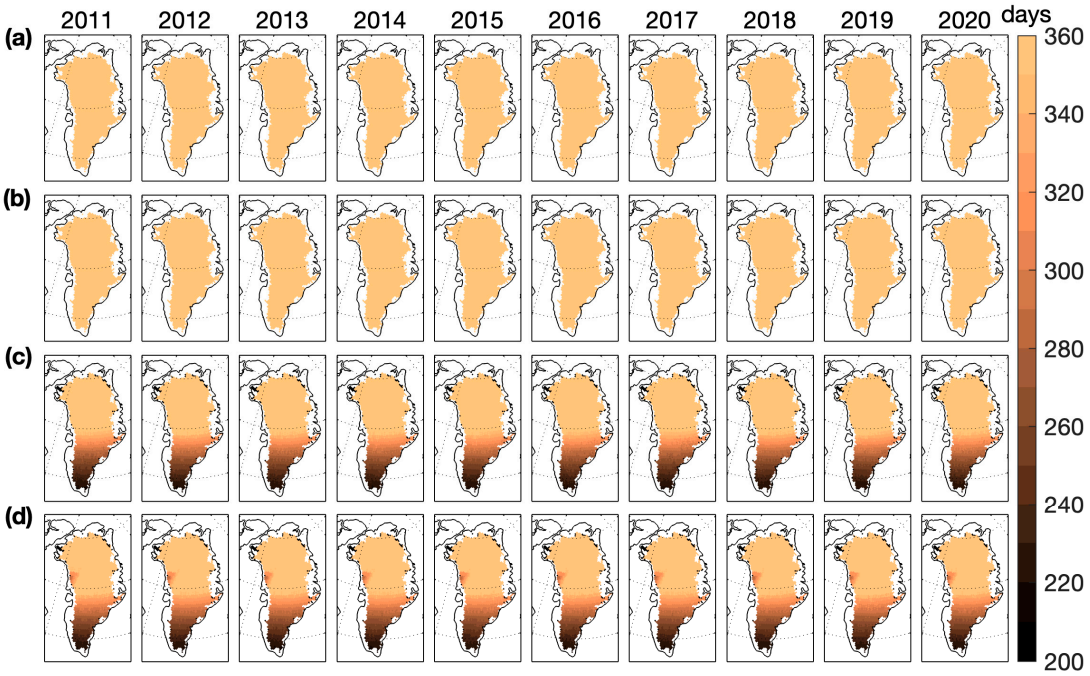

Figure 1. Effective days with passive microwave data. (**a**) DMSP morning data; (**b**) DMSP evening data; (**c**) SMOS morning data; (**d**) SMOS evening data.

2.1.2. AWSs and MODIS Data

Owing to the scarcity of quantitative data concerning the surface melting of the GrIS [26], temperature serves as the sole available metric for assessing this phenomenon [9]. In this research study, data from 42 AWSs were selected from two datasets: the Greenland Climate Network (GC-Net) [27] and the Greenland Ice Sheet Monitoring Project (PROMICE) (refer to Figure 2). Data from PROMICE stations were provided by the Geological Survey of Denmark and Greenland (GEUS) (accessible at http://www.promice.dk, accessed on 1 January 2024). In this study, we analyzed surface melt outcomes derived from DMSP and SMOS data by utilizing hourly site temperatures per day from 2011 to 2020. Given the occurrence of melting due to radiative forcing (solar radiation), melting processes also take place when the air temperature falls below 0 °C. Thus, for AWS air temperature, we established three melt thresholds of 0, −1, and −2 °C [8].

Previous studies have pointed out that the Moderate Resolution Imaging Spectroradiometer (MODIS) summer ice surface temperature is significantly correlated with the mean melting range of the GrIS [28]. Therefore, in this study, in addition to station temperature data, MODIS ice surface temperature data were also used. DMSP and SMOS satellite data were considered for certain time points and were evaluated with MODIS ice surface temperature data to further support the evaluation results of station-derived temperature data. MODIS ice surface temperature data from the dataset "Multilayer Greenland Ice Surface Temperature, Surface Albedo, and Water Vapor from MODIS, Version 1" are freely available on the EarthData website [29]. The dataset includes both ice surface temperature data and surface melt products derived from ice surface temperature, where the melt threshold is set to −1 °C; this is because the accuracy of ice surface temperature data is ±1 °C, and if it were set to 0 °C, there would be omissions [30]. Yu et al. [31] used the ice surface temperature data from AWSs to evaluate those from MODIS, and the results show that the latter has a cooling deviation of about 2~4 °C. Compared with the ablation data from the AWSs, the consistency of the melt results obtained by using MODIS at −1 °C is 41~61%. In this study, we used data from 2011 to 2018, as well as data from spring, summer, and autumn 2019, to evaluate the melt values of the passive microwave data from the two satellites.

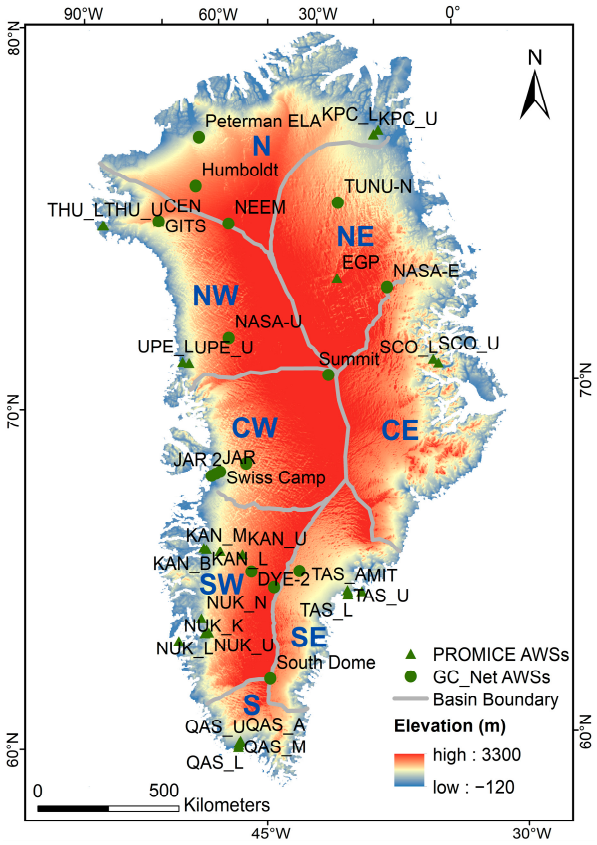

Figure 2. The distribution of the AWSs on the GrIS. The green dots represent the sites; the gray line represents the boundary line of the watershed; and the background color shows the elevation, with blue for low values and red for high values. The GrIS is divided into eight basins: northern (N), northwestern (NW), northeastern (NE), west-central (CW), east-central (CE), southwestern (SW), southeastern (SE), and southern (S).

The assessment data used in this study included site air temperature data and MODIS ice surface temperature data. The former data were obtained from both the GC_Net and PROMICE datasets. Tables 1 and 2 provide the number of valid days from 2011 to 2020 for the stations in both datasets. For a specific site, we may not necessarily have data for every year between 2011 and 2020, and for a specific year, a site may not necessarily provide temperature data for 365 or 366 days. Figure 3 provides the number of valid days with MODIS ice surface temperature data from 2011 to 2018, the average of which was 294 days. The number of valid days with MODIS ice surface temperature data was unevenly distributed across the various regions of Greenland (the number of valid days is higher in the north than in the south) (Figure 3). This is due to the fact that MODIS data are susceptible to cloud cover, which makes them unavailable in some areas.

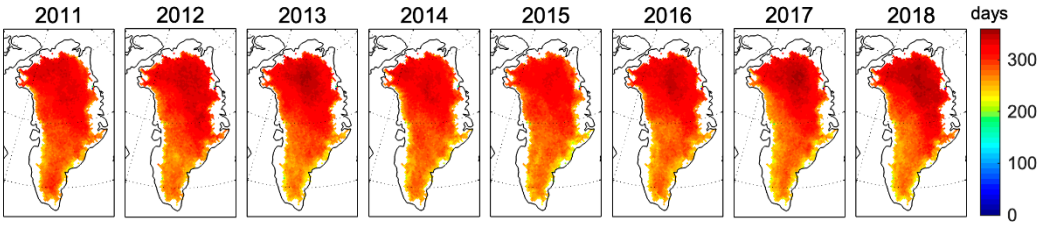

Figure 3. Number of valid days with MODIS ice surface temperature data.

Table 1. Number of valid days with AWS data from the GC_Net dataset.

Site\Year	2011	2012	2013	2014	2015	2016	2017	2018	2019	2020
Swiss Camp	366	365	365	365	366	331	365	306	0	0
Crawford Pt.	0	0	0	194	114	198	269	251	0	0
NASA-U	254	337	315	335	298	321	294	0	0	0
GITS	0	259	283	329	269	298	2	141	0	0
Humboldt	181	247	242	276	203	272	211	218	0	0
Summit	244	363	365	364	364	365	365	306	0	0
TUNU-N	180	326	364	365	366	365	306	0	0	0
DYE-2	366	365	365	365	366	229	283	306	0	31
JAR	219	202	291	170	263	331	182	185	0	0
Saddle	366	365	365	365	358	365	365	306	0	0
South Dome	329	365	365	365	366	365	365	306	0	0
NASA-E	366	365	365	365	366	365	306	0	0	0
NASA-SE	366	365	319	365	366	365	365	306	0	0
JAR 2	229	240	0	0	0	0	0	0	0	0
Peterman ELA	143	364	365	277	0	1	0	0	0	0
NEEM	366	365	365	365	365	365	327	253	0	0

Table 2. Number of valid days with AWS data from the PROMICE dataset.

Site\Year	2011	2012	2013	2014	2015	2016	2017	2018	2019	2020
KPC_L	0	225	365	365	366	365	365	365	241	145
KPC_U	366	365	365	365	366	240	325	365	241	145
EGP	0	0	0	0	0	270	365	365	241	145
SCO_L	366	365	365	365	366	365	365	365	366	184
SCO_U	366	365	365	240	323	365	365	365	366	184
MIT	366	365	365	365	365	365	240	200	200	145
TAS_L	262	365	365	365	365	164	217	365	366	184
TAS_U	366	242	365	365	92	0	0	0	0	0
TAS_A	0	0	181	365	366	365	365	303	366	184
QAS_L	356	365	365	365	364	365	365	365	241	145
QAS_M	0	0	0	0	0	56	296	365	366	184
QAS_U	356	365	365	365	366	365	365	365	241	145
QAS_A	0	15	197	346	0	0	0	0	0	0
NUK_L	315	365	365	365	366	365	365	365	366	184
NUK_U	326	365	287	230	297	365	365	365	366	184
NUK_K	0	0	0	181	366	365	365	365	366	184
NUK_N	289	326	365	92	0	0	0	0	0	0
KAN_B	274	365	365	365	366	365	365	365	366	184
KAN_L	366	365	365	365	366	365	365	365	366	184
KAN_M	366	365	307	258	366	365	365	365	364	184
KAN_U	240	365	365	365	366	365	365	365	366	184
UPE_L	366	356	365	365	366	365	365	365	366	184
UPE_U	366	365	365	365	347	365	365	365	366	184
THU_L	302	365	365	365	251	360	365	364	241	145
THU_U	259	365	365	365	366	365	365	365	205	145
CEN	0	0	0	0	0	0	220	365	241	145

It has been documented that the snowline of the GrIS experiences seasonal and interannual fluctuations, making it challenging to map [32]. Consequently, snowline vector data have not yet been disseminated on the official website. In the research study conducted by Ryan et al. [32], the mean snowline elevation data in eight regions of Greenland (north, northeast, east-central, southeast, south, southwest, west-central, and northwest (refer to Figure 2)) between 2001 and 2017 were determined. To investigate the correlation between the surface melt error distribution of the two passive microwave datasets and the altitude of the snowline, the average snowline altitude from 2011 to 2017 was utilized.

2.1.3. Sentinel-2 Imagery

Sentinel-2 data became available after 23 June 2015; therefore, in this study, we used data from each summer from 2016 to 2020, as well as Sentinel-2 top-of-atmosphere (TOA) reflectivity data, both synthetic and daily, for each summer. For the Sentinel-2 data, a total of five bands (B4: red band; B3: green band; B2: blue band; B10: cirrus band; B11: SWIR 1 band) were used, and their spatial resolutions were 10 m, 10 m, 10 m, 60 m, and 20 m, respectively. In GEE, the resolution of all bands is set to 10 m.

2.2. Methods

2.2.1. Surface Melt Simulation

MEMLS2 is a temperature threshold-based method proposed by Tedesco et al. [9]. Compared with other threshold methods, this algorithm not only exhibits heightened sensitivity to LWC but also demonstrates higher concurrence with surface melt estimates derived from AWS air temperature data, making it more suitable for simulating surface melt in Greenland [8]. Based on the Microwave Emission Model of Layered Snowpack (MEMLS), this method simulates the brightness temperature beneath a wet snow layer of the fixed thickness (5 cm) and liquid water content (0.2%), thereby obtaining a linear function of the melt threshold and winter brightness temperature, which is typically expressed as follows [9]:

$$Tc = \gamma * Twinter + \omega$$

where γ = 0.48, ω = 128 K, and Twinter represents the average brightness temperature in winter. The MEMLS incorporates specific parameter settings, which include snow density ranging from 0.1 to 0.45 g/cm^3, correlation length from 0.01 mm to 0.3 mm, and snow temperature between 230 K and 270 K. Each layer is 5 cm thick, accumulating a total thickness of 20 m. The bottom layer consists of ice, with a density of 0.917 g/cm^3.

Houtz et al. proposed a novel technique for simulating surface melt by employing the L-band-Specific Microwave Emission Model of Layered Snowpacks (LS-MEMLS) of stratified snow [12]. This innovative approach not only facilitates the calculation of the surface melting status but also offers the LWC of the GrIS's surface. In comparison with the brightness temperature threshold method, this technique demonstrates immense potential for estimating GrIS surface-derived mass loss. In the LS-MEMLS, initially, the known humidity and density values are simulated as the atmospheric bottom brightness temperature. Subsequently, the loss function of the simulated and satellite measurement-based brightness temperature is computed. The retrieval values of humidity and density within the snow cover on the ice sheet's surface are determined according to the minimum value of the loss function [12]. For the specific formula of this method, refer to the study by Houtz et al. [12], which is not to be reiterated here.

As in Colosio et al. [8], in this study, the same three metrics of overall accuracy (OA), commission error (CO), and omission error (OM) based on confusion matrices were chosen to characterize the accuracy of the surface melt results. The case where the AWS air temperature data (MODIS ice surface temperature data) indicated the presence of melt and the result calculated from the passive microwave data indicated its absence was categorized as an omission error (OM), while the case where the AWS air temperature data (MODIS ice surface temperature data) indicated the absence of melt and the result obtained from the passive microwave data indicated its presence was categorized as commission error (CO) [8].

2.2.2. Mapping of SGLs

Two indices, the modified Normalized Differential Water Index (NDWI) and the Normalized Differential Snow Index (NDSI), were used in this study. The former, proposed by Yang et al. [33], uses blue–red bands to extract water bodies. Compared with the traditional NDWI (using green waves and near-infrared bands), this index can enhance the spectral contrast of ice, snow, and water bodies. The NDSI, which uses both green

wave and shortwave infrared bands, can rule out the effect of rock [34,35]. In this study, we used a set of automatic water body extraction methods on Sentinel-2 images when extracting water bodies, as proposed by Moussavi et al. [36]. The rock mask was extracted by calculating NDSI < 0.85 and B2 < 0.4. The cloud mask was extracted by calculating B11 > 0.1 and B10 > 0.01. Then, NDWI > 0.18 and (B3–B4) > 0.09 were calculated to extract the water bodies. On the basis of water body extraction, the influence of rock and cloud could be excluded by applying rock and cloud masks, respectively. Image downloading and water extraction operations were all carried out on the GEE platform [37]. Figure 4 shows the flow chart of the processing of data and analysis of results in this study.

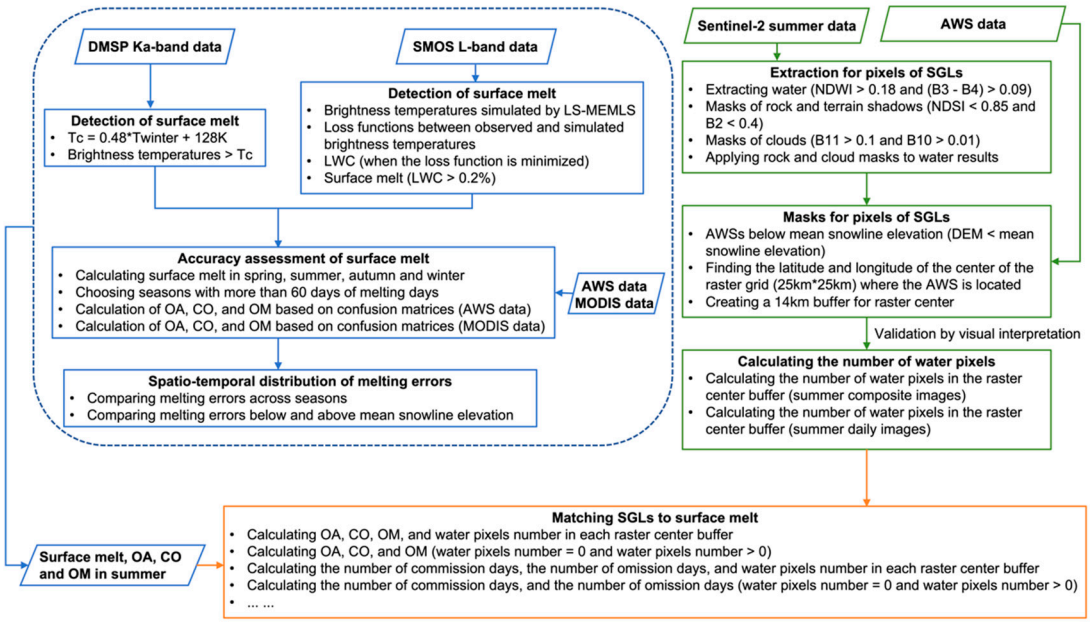

Figure 4. Technical flowchart of this study.

3. Results

3.1. Spatio-Temporal Distribution of Surface Melt and Surface Melt Errors

3.1.1. In Ka Band

In this research study, we employed DMSP morning and evening data to determine the duration of the melting of the GrIS during spring, summer, autumn, and winter, spanning the years 2011 to 2020 (refer to Figure 5a,b). The number of melt days in each season varied in the range of [0, 92] days. In order to facilitate a more visually striking depiction of the melting range, we assigned the grids with zero-day melting period Not a Number (NaN) values, which are accordingly represented as blank spaces in the graphs below. The DMSP data failed to detect any melting during the winter season, indicating that the number of days with melting at each location was nil. Consequently, the duration of the melting process in winter is not displayed. The grids with less melting are depicted in blue, and those with frequent melting are in red. In the spring season, melting was merely observed in the peripheral regions of the GrIS, with the corresponding melt day values being relatively low (displayed in blue in the graphs). In the summer season, the frequency of melt events generally decreased from the peripheral regions of Greenland towards its interior regions, as illustrated by the color gradient from red to yellow, green, blue, and blank in the figure. The years 2012 and 2019 were characterized by extreme melting, which was detected across the majority of Greenland's surface (refer to Figure 5a). In autumn, melting was solely detected within the peripheral regions of SW and SE Greenland, with the number of melt days being exceedingly low (represented in blue within the illustration). Melting was found to demonstrate distinct seasonal and vertical disparities and primarily occurred during the summer season.

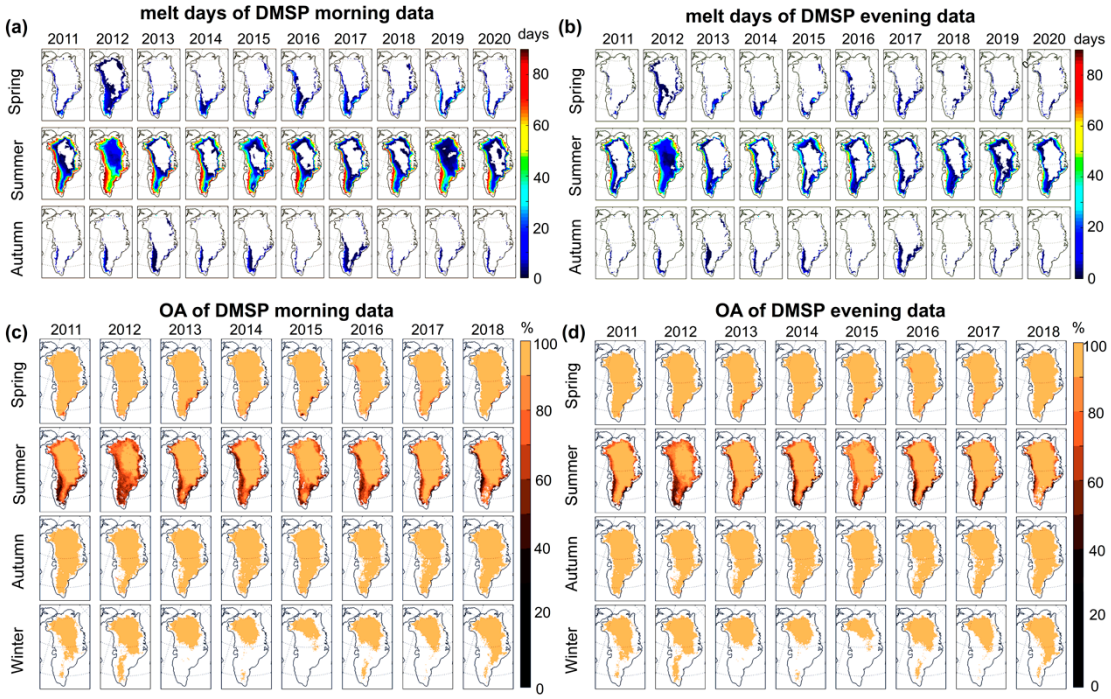

Figure 5. Melt days and overall accuracy of DMSP data. (**a**,**b**) represent the melt days of DMSP morning and evening data, respectively, in spring, summer, and autumn (2011–2020); (**c**,**d**) denote the OA values of DMSP morning and evening data, respectively, in spring, summer, autumn, and winter. The blank areas indicate NaN values.

The discrepancy between the DMSP morning and evening data regarding melt results was more pronounced during the summer season. For instance, in this season, from 2011 to 2020, a distinct reddish hue is evident in Figure 5a, while only a limited amount of such coloration is observed along the periphery of Greenland in Figure 5b. In 2019, the DMSP morning data revealed melting across the whole region (refer to Figure 5a); however, the DMSP evening data did not indicate the occurrence of any melting within the high-altitude inner regions (see Figure 5b). The DMSP morning data suggested a wider range of melt occurrences and a higher melt day number than the DMSP evening data.

In this research study, we assessed the surface melt results identified by using DMSP data and compared them with those estimated derived from AWS air temperatures and MODIS ice surface temperature data. For a designated AWS or grid, we calculated accuracy metrics (OA, CO, and OM) for DMSP data for spring, summer, autumn, and winter. We then computed the mean values of the data across all AWSs and grids, taking into account the season and the mean snowline elevation. Table 3 presents the precision metrics for DMSP data across different seasons and altitudes, including spring, summer, autumn, winter, and above and below the snowline. The OA for the DMSP data in spring, autumn, and winter exceeded 90%. However, in summer, this metric decreased to approximately 76% (according to the AWS data) or 83% (according to the MODIS data). It appears that the inaccuracies in DMSP-based melt detection were primarily concentrated during the summer season. Above the average snowline altitude, the OA of the DMSP data exceeded 94%, whereas below the average snowline altitude, it ranged from 84% to 89%. This indicates that the surface melt error of the DMSP data was mainly concentrated below the mean snowline elevation. Figure 5c,d display the spatio-temporal distribution of the OA values derived from the DMSP data. In terms of temporal scale, the minimal values of the OA of DMSP data were primarily observed during the summer season, and in terms of spatial scale, they predominantly corresponded to the peripheral regions of Greenland at relatively low altitudes.

Table 3. Accuracy results for DMSP data in spring, summer, autumn, winter, and both above and below mean snowline elevation, including assessment data from AWSs and MODIS (The word "\" in the table represents the null value).

Assessment Data	Season\Altitude	DMSP Morning Data			DMSP Evening Data		
		OA (%)	CO (%)	OM (%)	OA (%)	CO (%)	OM (%)
AWSs	Spring	92	7	42	93	2	80
	Summer	77	40	19	74	15	55
	Autumn	93	1	67	91	1	85
	Winter	99	0	97	99	0	87
	Above the snowline	94	5	39	96	1	82
	Below the snowline	86	20	45	84	8	68
MODIS	Spring	98	2	35	99	1	88
	Summer	82	23	19	84	11	68
	Autumn	99	0	75	100	0	92
	Winter	100	0	\	100	0	\
	Above the snowline	96	11	67	97	6	90
	Below the snowline	89	20	53	88	13	78

During the summer months, the CO was 21% (AWS-based data) or 4% (MODIS-based data) higher than the OM for the DMSP morning data, and the OM was 40% (AWS-based data) or 57% (MODIS-based data) higher than the CO for the DMSP evening data (Table 3). This indicates that the DMSP morning data are susceptible to commission errors during the summer months, while the DMSP evening data are likely to experience omission errors. This observation is further corroborated by the data presented in Figure 5a,b.

3.1.2. In L Band

In this research study, we employed SMOS data to determine the duration of the melting of the GrIS in spring, summer, autumn, and winter, spanning the years 2011 to 2020 (refer to Figure 6a,b). The illustration below shows a color-coded representation of the melt days, with blue indicating low values, red indicating high values, and grids with 0 melt days being designated as NaN values and displayed as empty spaces. In spring, melting was observed in the peripheral regions of Greenland, characterized by a high number of melt days (represented in red in the plots). Simultaneously, the melting detected in the interior regions of Greenland displayed a low number of melt days (illustrated in blue in the plots). The degree of melting and the number of melt days displayed by the SMOS data were significantly higher in the summer than in the spring. The spatial distribution pattern of melt days, according to the SMOS data, in autumn and winter was quite similar to that in spring. The findings indicate that the substantial melting indicated by the SMOS data was primarily concentrated in the peripheral regions of Greenland.

The spatial distribution patterns of melt days indicated by the SMOS morning and evening data exhibited a high degree of similarity (Figure 6a,b). Nonetheless, in 2011, within the interior of northern Greenland, the number of melt days indicated by the SMOS morning data was consistently low (depicted in blue in Figure 6a), whereas the number of melt days indicated by the SMOS evening data was elevated (illustrated in red in Figure 6b).

By employing the estimated surface melt results derived from AWS air temperature and MODIS ice temperature data as a reference, in this research study, we assessed the surface melt results identified by using the SMOS data (refer to Table 4). These data exhibited the highest OA, 68%, with respect to AWS air temperature data and the lowest OA, 85%, with respect to MODIS ice surface temperature data, both during the summer. This discrepancy is presumably attributed to the paucity of available AWSs. Upon evaluation of the AWS data, it was found that the SMOS data exhibited an OA of over 90% at elevations above the average snowline; conversely, at elevations below the average snowline, this metric was approximately 36%. When we performed the evaluation with the MODIS data, at elevations above the average snowline, the OA value of the SMOS data exceeded

90%, whereas at elevations below the average snowline, it was approximately 70%. These findings indicate that the inaccuracies in surface melt identified by using the SMOS data primarily concern the summer season and altitudes below the average snowline.

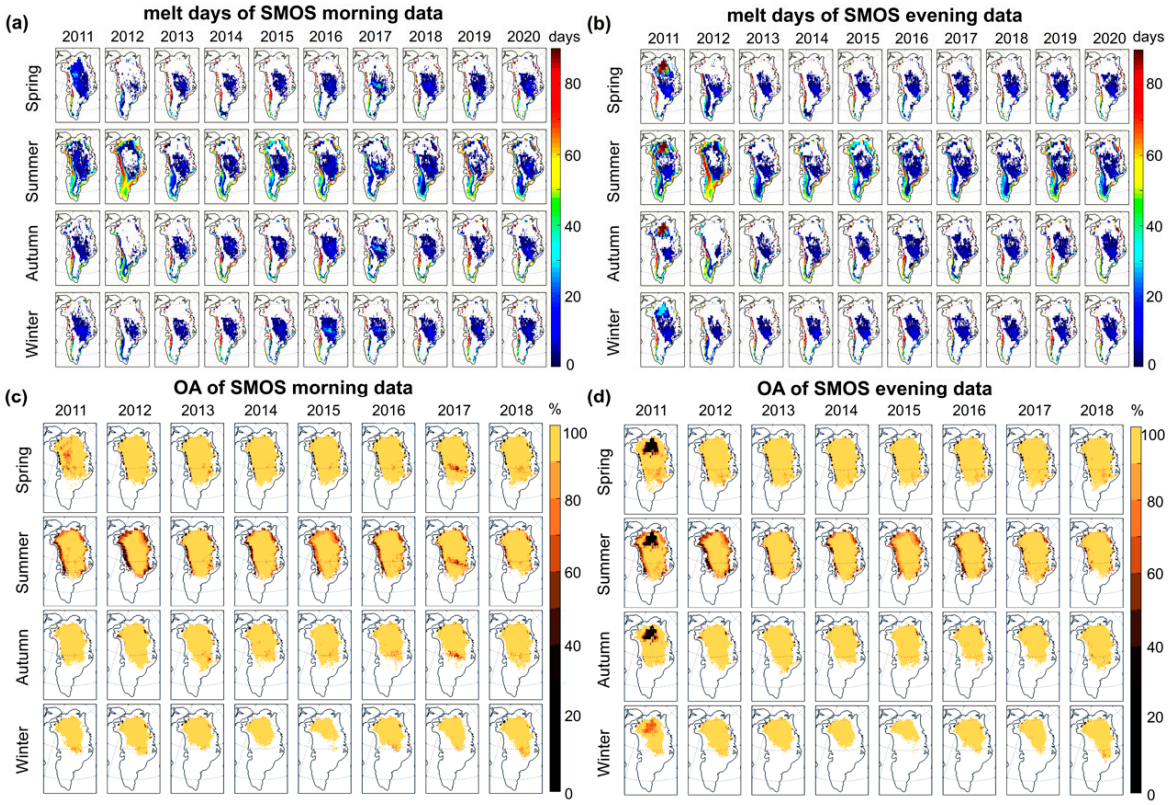

Figure 6. Melt days and overall accuracy of SMOS data. (**a**,**b**) represent the number of melt days according to SMOS morning and evening data, respectively, in spring, summer, autumn, and winter (2011 to 2020); (**c**,**d**) indicate the OA values according to SMOS morning and evening data, respectively, in spring, summer, autumn, and winter, with the blank areas denoting NaN values.

Table 4. Accuracy results for SMOS data in spring, summer, autumn, winter, and both above and below the mean snowline elevation, including evaluation data from AWSs and MODIS (The word "\" in the table represents the null value).

Assessment Data	Season\Altitude	SMOS Morning Data			SMOS Evening Data		
		OA (%)	CO (%)	OM (%)	OA (%)	CO (%)	OM (%)
AWSs	Spring	64	35	53	63	36	59
	Summer	69	35	57	67	33	61
	Autumn	65	36	43	65	36	45
	Winter	61	38	54	62	37	36
	Above the snowline	94	5	77	93	5	77
	Below the snowline	36	68	46	36	66	45
MODIS	Spring	92	8	69	91	9	79
	Summer	85	15	71	84	17	63
	Autumn	95	5	81	94	6	96
	Winter	95	5	\	95	5	\
	Above the snowline	95	14	92	94	15	89
	Below the snowline	69	57	80	70	57	74

Figure 6c,d display the spatial distribution of the OA values derived from the SMOS data across Greenland. In the figure, higher OA values are illustrated in yellow and lower

OA values in black. It can be observed that the minimal OA values of the SMOS data primarily concern the summer season and the peripheral regions of Greenland. The spatial distribution patterns of the OA values of the SMOS morning and evening data exhibited a high degree of similarity, with only the inland regions of northern Greenland demonstrating notable disparities in 2011.

3.2. Spatio-Temporal Variation of SGLs

The occurrence of surface melt errors in the Ka and L bands was primarily concentrated during the summer season and below the mean snowline elevation (Section 3.1). Therefore, in this research study, by utilizing the water body identification approach detailed in Section 2.2.2, we successfully extracted the SGL water body pixels within the summer composite image (median composite) spanning 2016 to 2020. We identified the latitude and longitude coordinates of the center of the grids (25 km × 25 km) where the AWSs below the mean snowline elevation were situated. Subsequently, a 14 km buffer zone was established for these centroids, and the number of SGL water body pixels within the buffer zone was tallied (Table 5). From 2016 to 2020, the maximum number of water bodies was observed in the grids where UPE_U, JAR, KAN_M, KAN_M, and JAR were situated, respectively. Figure 7 illustrates the water bodies situated within the buffer zone encompassing the centroids of these grids. For each grid where the sites were located, the number of water body pixels per day was also calculated for the summer months of 2016 to 2020. Figure 8 shows the results of water body pixel extraction for each day in the summer of 2016 for the grid where UPE_U was located. It can be noticed that the SGL water bodies in the summer were in a dynamic state of flux.

In 2016, the total number of water bodies exceeded 1000, including those in the Swiss Camp, JAR, KAN_L, KAN_M, UPE_L, and UPE_U grids, where the AWSs were situated. The research results confirm the accuracy of daily SGL water body identification in the aforementioned grids. The boundaries of the SGLs were manually delineated on Sentinel-2 summer synthetic imagery, and a 200 m buffer zone was established for them. Subsequently, two water sample points were randomly chosen within the SGLs' perimeter, along with two non-water sample points within the buffer zones, as illustrated in Figure 9. A comprehensive study involving the selection of a total of 168 sample points, which included 84 water-body samples and an equal number of non-water-body samples, was conducted. Confusion matrices were calculated by examining the imagery for each day of summer (within the above-mentioned six grids). The overall accuracy reached a desirable value of 96%, accompanied by a Kappa coefficient of 0.92. This demonstrates that the water bodies analyzed in this research study yielded satisfactory outcomes.

Table 5. Total number of pixels of SGL water bodies was calculated within a 14 km buffer zone in the center of grids where AWS's average snowline elevation was situated. Analysis based on Sentinel-2 summer composite imagery spanning from 2016 to 2020.

Site\Year	2016	2017	2018	2019	2020
Swiss Camp	10,752	97	0	18,840	294
JAR	8000	10,894	0	2985	4210
JAR2	8000	10,894	0	2985	4210
Peterman ELA	12	0	0	0	0
KPC_U	0	0	0	0	0
TAS_L	63	0	0	0	0
TAS_U	63	0	0	0	0
TAS_A	63	0	0	0	0
QAS_U	30	0	0	16	0
QAS_A	0	89	0	751	0
NUK_U	296	1058	0	464	12
NUK_N	571	983	0	444	0
KAN_L	2144	2910	756	1948	111

Table 5. *Cont.*

Site\Year	2016	2017	2018	2019	2020
KAN_M	30,609	1905	3019	32,175	901
UPE_L	2278	23	0	508	65
UPE_U	46,623	564	0	16,941	52
THU_L	0	0	0	0	0
THU_U	0	0	0	0	0

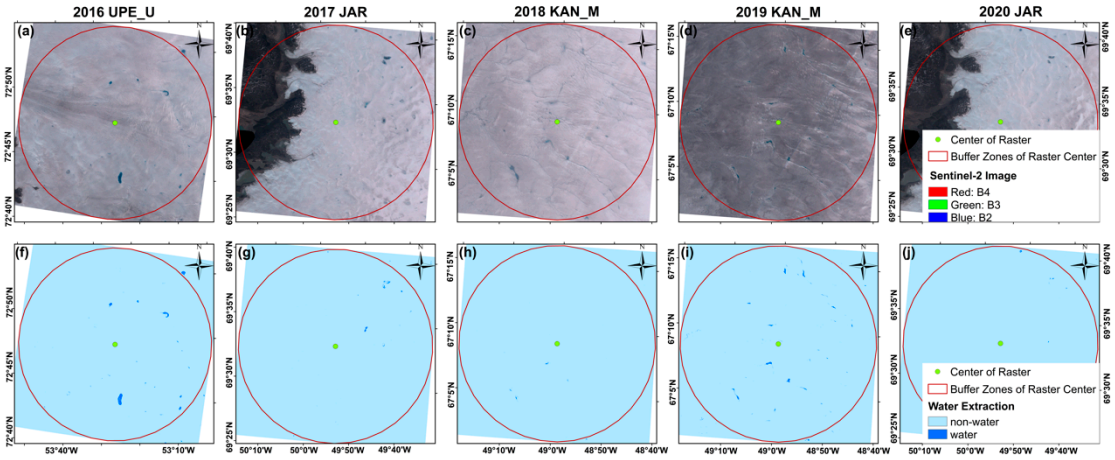

Figure 7. Extraction results of SGL water body pixels. (**a**–**e**) represent Sentinel-2 summer synthetic images from 2016 to 2020, respectively, allocated in grids (25 km × 25 km) where AWSs (UPE_U, JAR, KAN_M, KAN_M, and JAR, respectively) were situated. (**f**–**j**) depict water body extraction outcomes of Sentinel-2 images at corresponding grids from 2016 to 2020, respectively. Green dot: center of the grid where AWS is positioned; red boundary: 14 km buffer in the center of the grid; dark blue area: water body pixels; light blue section: non-water body pixels.

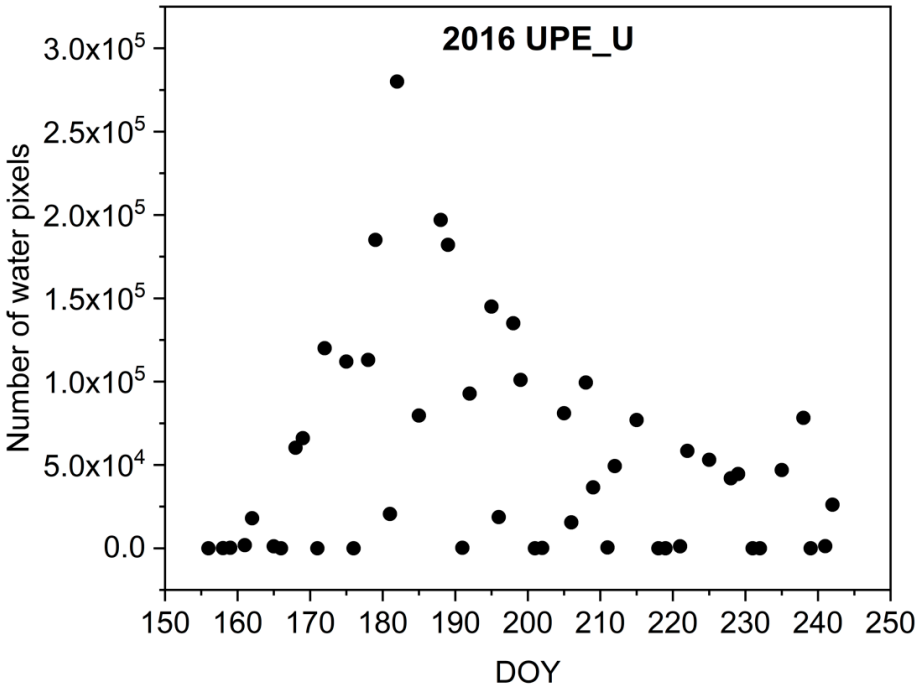

Figure 8. Number of water body pixels per day during the summer of 2016 in a grid where UPE_U was located. The horizontal coordinate represents the day of the year, and the vertical coordinate represents the number of water body pixels.

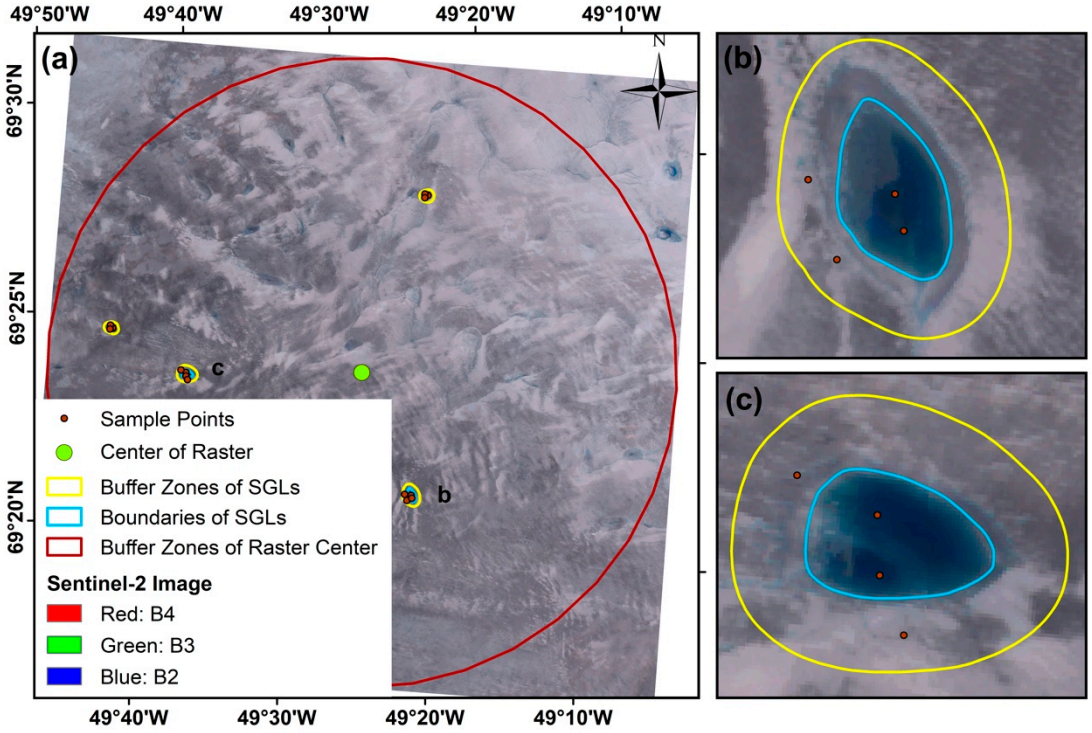

Figure 9. Sample point selection. (**a**) A synthetic image relative to the 2016 Sentinel-2 summer season within the grid where Swiss Camp was situated; the green point represents the center of the grid, the red point signifies the selected sample point, the red boundary denotes the 14 km buffer zone in the center of the grid, the blue boundary represents the artificially mapped boundary of the SGLs, and the yellow boundary indicates the 200 m buffer zone. (**b**,**c**) depict magnified views of the two SGLs in Figure (**a**), respectively.

3.3. Effect of SGLs on Surface Melt Data Inversion

3.3.1. On Ka Band

In this research study, we calculated not only the count of SGL water bodies within the grids where the AWSs were located (in summer synthetic imagery) but also the accuracy metrics (OA, CO, and OM) for the DMSP data within these specific grids. Using grids facilitates the correlation between the surface melt error in the Ka band and the count of SGL water body pixels. The accuracy metrics of the DMSP data were categorized into two groups based on the "water body pixel number = 0" and "water body pixel number > 0" criteria (Table 6) for the summer synthetic imagery. It was observed that the presence of SGL water body pixels led to 36% and 20% increases in the CO of the DMSP morning and evening data, respectively.

Table 6. The accuracy results of the DMSP data in both SGL and non-SGL environments. The SGL water bodies in this study were derived from Sentinel-2 summer synthetic imagery.

Water Body Pixel Number	DMSP Morning Data			DMSP Evening Data		
	OA	CO	OM	OA	CO	OM
=0	61%	36%	39%	44%	12%	66%
>0	76%	72%	4%	72%	32%	27%

For each grid encompassing an AWS area for a specific summer day, we computed the number of water body pixels and ascertained whether they had been erroneously categorized or overlooked based on the air temperature registered by the AWS and the surface melt indicated by the DMSP data. We also meticulously calculated the number of summer days for which this parameter had been misclassified and overlooked by using the

DMSP data based on the "water body pixel number = 0" and "water body pixel number > 0" criteria (refer to Table 7). The number of days with CO increased by 12 and 3 days when using the DMSP morning and evening data, respectively, when SGL water body pixels were present.

Table 7. Days with misclassification and omission errors with the use of DMSP data in the absence and presence of SGL water bodies. The SGL water bodies here were derived from daily Sentinel-2 imagery.

Water Body Pixel Number	DMSP Morning Data		DMSP Evening Data	
	Days with CO	Days with OM	Days with CO	Days with OM
=0	14	21	5	42
>0	26	3	8	17

Furthermore, we calculated the corresponding number of water bodies for each day and the disparity between TB and Tc in instances where the surface melt indicated by the DMSP data was truly negative, truly positive, misclassified, or overlooked (refer to Figure 10). When the DMSP data did not indicate surface melt (TN), the number of SGL water bodies was low; when these data indicated surface melt (TP), this number was high. The presence of strong surface melt suggests that SGLs are equally well developed. When the DMSP data indicated surface melt (CO), the number of SGL water bodies was high; when these data did not indicate surface melt (OM), this number was low. This suggests that the elevated brightness temperature in the DMSP data could be attributed to a combination of surface melt and SGLs. A situation where the surface melt is absent but the SGL water body number remains high can also lead to the DMSP data's brightness temperature surpassing the melt threshold, resulting in a commission error. When surface melting occurs but the SGL water body number is lower, this results in the DMSP data's brightness temperature falling below the melt threshold, leading to an omission error.

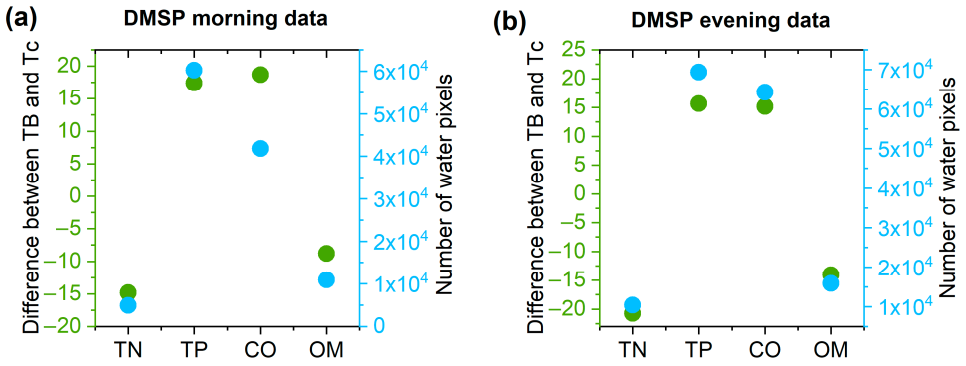

Figure 10. Number of SGL water body pixels (right y-axis) with the difference between brightness temperature and melting threshold data (left y-axis) based on surface melt indicated by DMSP data, categorized into true negatives, true positives, commission error, and omission error. (**a**) DMSP morning data; (**b**) DMSP evening data.

3.3.2. On L Band

We further evaluated the precision outcomes of the SMOS data in the absence and presence of SGLs (Table 8). It can be observed that the percentage of OM in the SMOS morning and evening data increased by 33% and 32%, respectively, when SGLs were present. In addition, we also calculated the number of days with CO and OM for the SMOS data in the presence and absence of SGLs (Table 9). When SGLs were present, the number of days with OM for the SMOS morning and evening data increased by 17 and 21 days, respectively. This indicates that the presence of SGLs increases the omission error of SMOS data.

Table 8. The accuracy results of the SMOS data in both SGL and non-SGL environments. The SGL water bodies in this study were derived from Sentinel-2 summer synthetic imagery.

Water Body Pixel Number	SMOS Morning Data			SMOS Evening Data		
	OA	CO	OM	OA	CO	OM
=0	66%	68%	26%	69%	77%	27%
>0	43%	65%	59%	41%	57%	59%

Table 9. The number of days with CO and OM for the SMOS data in the absence and presence of SGL water bodies. The SGL water bodies here were derived from daily Sentinel-2 imagery.

Water Body Pixel Number	SMOS Morning Data		SMOS Evening Data	
	Days with CO	Days with OM	Days with CO	Days with OM
=0	21	11	15	13
>0	17	28	10	34

We calculated the number of SGL water bodies and the disparity between the actual LWC and the model 0.2% LWC when the surface melt result indicated by the SMOS data was truly negative, truly positive, misclassified, and overlooked (Figure 11). In general, the number of SGLs was consistent with the intensity of the LWC indicated by the SMOS data. Although the presence of SGLs was found to increase the omission error of the SMOS data, the occurrence of omission was not in a one-to-one response relationship with the presence of SGLs. Moreover, there was no linear relationship between the LWC determined according to the SMOS data and the number of SGL water bodies.

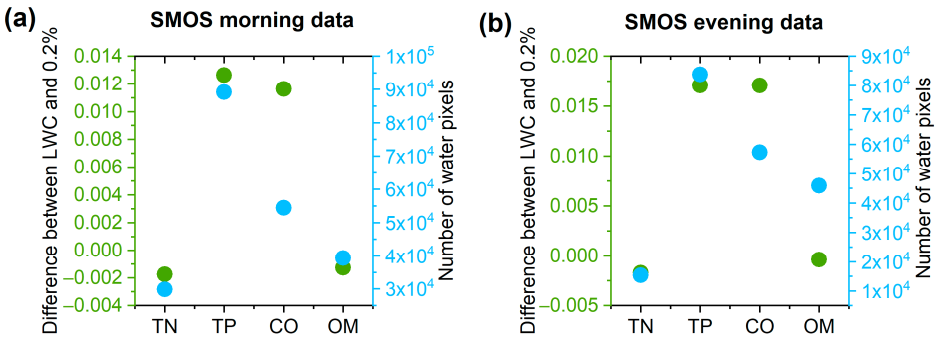

Figure 11. The number of SGL water bodies (right y-axis) and the difference between the actual LWC and the model 0.2% LWC (left y-axis) for surface melt are indicated by the SMOS data as truly negative, truly positive, misclassified, and overlooked. (**a**) SMOS morning data; (**b**) SMOS evening data.

4. Discussion

The DMSP Ka-band detected extreme surface melting during the summers of 2012 and 2019 (refer to Figure 5a,b). By applying data from three different sensors, Nghiem et al. found that the melting extent in Greenland was as high as 98.6% on 12 July 2012 [10]. Zheng et al. combined a combination of regional climate models, passive microwave data, and machine learning to find melting across Greenland in mid-July 2012 [38]. The extreme melting event in July 2012 may be related to anomalous warm air ridges due to high blockages in Greenland [10]. In 2019, the surface mass balance, snowfall, and runoff set new records, and anomalously persistent anticyclones, low snowfall, and low albedo promoted the absorption of solar radiation and enhanced surface melting [39]. Extreme melting in 2019 may be related to anomalous atmospheric conditions [39]. This suggests that the surface melting detected by the DMSP Ka-band is in good agreement with previous studies.

Surface melting is generally more prevalent in the summer, while it is scarcely observed or altogether nonexistent during the non-melting seasons, i.e., spring, autumn, and winter. Nonetheless, for periods devoid of surface melting, the SMOS data revealed the occurrence of melting in the GrIS's marginal and inland regions (refer to Figure 6a,b). Previous research has indicated that the SMOS satellite may exhibit false positives during the non-melting seasons. For instance, when Houtz et al. employed SMOS L-band data to identify liquid water in Greenland, they discovered a notable non-zero liquid water column during the dry snow season in 2016 [11]. The L band exhibits significant penetration capabilities in snowy environments, and its false-positive retrieval during non-melting seasons may be attributed to the presence of buried lakes and firn aquifers within the GrIS during winter [11]. Zheng et al. discovered buried lakes between 2017 and 2022, which were primarily located in west-central, southwestern, and northeastern Greenland, at elevations ranging from 800 to 1700 m [40]. Shang et al. investigated firn aquifers during the 2010–2020 period and discovered that they were primarily situated in southeastern and southern Greenland [41].

When snow melting occurs, the presence of liquid water content changes the dielectric constant and emissivity of snow, which ultimately leads to a change in brightness temperature, which can be captured with microwave radiometers [7]. However, the change in liquid water content is not simply linearly related to the change in brightness temperature [38]. The increase in liquid water content before the snowpack layer reaches saturation is manifested as an increase in brightness temperature in microwave radiometer-based data [7]. Therefore, existing surface melt algorithms essentially allow for the detection of liquid water content in the snowpack layer through a sharp change in brightness temperature [7]. The snowpack layer has a high albedo, typically above 0.8 [42]. SGLs, on the other hand, have lower albedos, usually below 0.3 [43]. This allows SGLs to absorb more solar radiation than snow, increasing their own temperature and promoting the melting of the surrounding snow and ice [44]. The positive albedo feedback of SGLs may allow the relevant pixels in the grid to have greater Ka-band thermal emission, presenting a higher brightness temperature in microwave radiometer data, leading to the false-positive retrieval of surface melt in the Ka band (Section 3.3.1). L-band microwave radiometers detect brightness temperatures from glacial ice, wet snow, and atmospheric thermal radiation [12]. L-band penetration depth ranges from 15 to 120 m in ice, >100 m in dry snow, and >1.8 m in wet snow (<1% LWC); however, penetration depth in water is of the order of 1 cm [45–47]. Therefore, when SGLs are present, microwave radiometers may not detect L-band brightness temperatures, resulting in the false negative retrieval of surface melt in the L band (Section 3.3.2).

In this study, the effect of SGLs on the passive microwave inversion of surface melt data was determined in terms of AWS temperatures (Section 3.3). Due to the lack of measured data for the GrIS, the use of station temperatures to evaluate the results of remote sensing has so far been considered a good means of assessment [9]. Previous studies have shown that site air temperature varies from −10 °C to 10 °C during ice sheet melting at different locations [48]. In this study, for site air temperatures, we only used three melt thresholds, i.e., −0, −1, and −2 °C. We found that the commission and omission error of the inversion of surface melt data in two bands decreased and increased, respectively, when the melt threshold for site air temperature was lowered from 0 °C to −2 °C. Therefore, for site air temperature, if a lower melt threshold, i.e., below −2 °C, is used, the effect of SGLs on the commission error in the Ka band may decrease, and that on the omission error in the L band may increase.

5. Conclusions

In this study, we quantified the seasonal surface melting of the Greenland Ice Sheet between 2011 and 2020 by utilizing DMSP and SMOS data. It was determined that the surface melt determined with Ka-band and L-band inversion was primarily concentrated during the summer and below the average snowline elevation. Subsequently, by utilizing the surface melt estimation derived from AWS air temperature and MODIS ice surface temperature data as a baseline, we identified that the surface melt errors in the Ka and

L bands were also predominantly concentrated during the summer and below the mean snowline elevation. Therefore, we selected AWSs situated below the mean snowline elevation, and by employing Sentinel-2 data from the summers of 2016 to 2020, we extracted SGL water body pixels in their vicinity and calculated the surface melt in the area with Ka-band and L-band data. By comparing the surface melt estimated from AWS air temperature data with that obtained with remote sensing data inversion, it was found that where SGLs were present, the DMSP morning and evening data had increases of 36% and 30% in CO, respectively, and of 12 and 3 days in the number of days with commission error, respectively; the SMOS morning and evening data had increases of 33% and 32% in OM, respectively, and of 17 and 21 days in the number of days with omission error, respectively. In future studies, we will delve deeper into the physical mechanisms by which SGLs influence melt data through passive microwave inversion by integrating Ka- and L-band surface melt results to minimize their impact and improve accuracy.

Author Contributions: Conceptualization, M.D.; Methodology, C.W.; Writing—original draft, Q.L.; Supervision, L.A.; Funding acquisition, M.D. All authors have read and agreed to the published version of the manuscript.

Funding: This study was supported by the National Science Foundation of China (grant No. 42122047), the National Key Research and Development Program of China (2021YFC2802504), and the Basic Fund of the Chinese Academy of Meteorological Science (grant No. 2024Z007 and 2023Z015).

Data Availability Statement: The data from the Programme for Monitoring of the Greenland Ice Sheet of the Geological Survey of Denmark and Greenland and from the Greenland Analogue Project were retrieved from http://www.promice.dk, accessed on 1 January 2024.

Conflicts of Interest: The authors declare no conflict of interest.

References

1. Morlighem, M.; Williams, C.N.; Rignot, E.; An, L.; Arndt, J.E.; Bamber, J.L.; Catania, G.; Chauché, N.; Dowdeswell, J.A.; Dorschel, B.; et al. BedMachine v3: Complete Bed Topography and Ocean Bathymetry Mapping of Greenland From Multibeam Echo Sounding Combined With Mass Conservation. *Geophys. Res. Lett.* **2017**, *44*, 11,051–11,061. [CrossRef] [PubMed]
2. Mouginot, J.; Rignot, E.; Bjørk, A.A.; van den Broeke, M.; Millan, R.; Morlighem, M.; Noël, B.; Scheuchl, B.; Wood, M. Forty-six years of Greenland Ice Sheet mass balance from 1972 to 2018. *Proc. Natl. Acad. Sci. USA* **2019**, *116*, 9239–9244. [CrossRef] [PubMed]
3. Shepherd, A.; Ivins, E.; Rignot, E.; Smith, B.; van den Broeke, M.; Velicogna, I.; Whitehouse, P.; Briggs, K.; Joughin, I.; Krinner, G.; et al. Mass balance of the Greenland Ice Sheet from 1992 to 2018. *Nature* **2020**, *579*, 233–239. [CrossRef] [PubMed]
4. Aschwanden, A.; Brinkerhoff, D.J. Calibrated Mass Loss Predictions for the Greenland Ice Sheet. *Geophys. Res. Lett.* **2022**, *49*, e2022GL099058. [CrossRef]
5. Choi, Y.; Morlighem, M.; Rignot, E.; Wood, M. Ice dynamics will remain a primary driver of Greenland ice sheet mass loss over the next century. *Commun. Earth Environ.* **2021**, *2*, 26. [CrossRef]
6. van den Broeke, M.; Box, J.; Fettweis, X.; Hanna, E.; Noël, B.; Tedesco, M.; van As, D.; van de Berg, W.J.; van Kampenhout, L. Greenland Ice Sheet Surface Mass Loss: Recent Developments in Observation and Modeling. *Curr. Clim. Change Rep.* **2017**, *3*, 345–356. [CrossRef]
7. Picard, G.; Leduc-Leballeur, M.; Banwell, A.F.; Brucker, L.; Macelloni, G. The sensitivity of satellite microwave observations to liquid water in the Antarctic snowpack. *Cryosphere* **2022**, *16*, 5061–5083. [CrossRef]
8. Colosio, P.; Tedesco, M.; Ranzi, R.; Fettweis, X. Surface melting over the Greenland ice sheet derived from enhanced resolution passive microwave brightness temperatures (1979–2019). *Cryosphere* **2021**, *15*, 2623–2646. [CrossRef]
9. Tedesco, M. Assessment and development of snowmelt retrieval algorithms over Antarctica from K-band spaceborne brightness temperature (1979–2008). *Remote Sens. Environ.* **2009**, *113*, 979–997. [CrossRef]
10. Nghiem, S.V.; Hall, D.K.; Mote, T.L.; Tedesco, M.; Albert, M.R.; Keegan, K.; Shuman, C.A.; DiGirolamo, N.E.; Neumann, G. The extreme melt across the Greenland ice sheet in 2012. *Geophys. Res. Lett.* **2012**, *39*. [CrossRef]
11. Houtz, D.; Mätzler, C.; Naderpour, R.; Schwank, M.; Steffen, K. Quantifying Surface Melt and Liquid Water on the Greenland Ice Sheet using L-band Radiometry. *Remote Sens. Environ.* **2021**, *256*, 112341. [CrossRef]
12. Houtz, D.; Naderpour, R.; Schwank, M.; Steffen, K. Snow wetness and density retrieved from L-band satellite radiometer observations over a site in the West Greenland ablation zone. *Remote Sens. Environ.* **2019**, *235*, 111361. [CrossRef]
13. Mousavi, M.; Colliander, A.; Miller, J.Z.; Entekhabi, D.; Johnson, J.T.; Shuman, C.A.; Kimball, J.S.; Courville, Z.R. Evaluation of Surface Melt on the Greenland Ice Sheet Using SMAP L-Band Microwave Radiometry. *IEEE J. Sel. Top. Appl. Earth Obs. Remote Sens.* **2021**, *14*, 11439–11449. [CrossRef]

14. Colliander, A.; Mousavi, M.; Marshall, S.; Samimi, S.; Kimball, J.S.; Miller, J.Z.; Johnson, J.; Burgin, M. Ice Sheet Surface and Subsurface Melt Water Discrimination Using Multi-Frequency Microwave Radiometry. *Geophys. Res. Lett.* **2022**, *49*, e2021GL096599. [CrossRef]
15. Mätzler, C.; Wiesmann, A. Extension of the microwave emission model of layered snowpacks to coarse-grained snow. *Remote Sens. Environ.* **1999**, *70*, 317–325. [CrossRef]
16. Schwank, M.; Rautiainen, K.; Mätzler, C.; Stähli, M.; Lemmetyinen, J.; Pulliainen, J.; Vehviläinen, J.; Kontu, A.; Ikonen, J.; Ménard, C.B. Model for microwave emission of a snow-covered ground with focus on L band. *Remote Sens. Environ.* **2014**, *154*, 180–191. [CrossRef]
17. Braithwaite, R.J.; Laternser, M.; Pfeffer, W.T. Variations of near-surface firn density in the lower accumulation area of the Greenland ice sheet, Pâkitsoq, West Greenland. *J. Glaciol.* **1994**, *40*, 477–485. [CrossRef]
18. Hu, J.; Huang, H.; Chi, Z.; Cheng, X.; Wei, Z.; Chen, P.; Xu, X.; Qi, S.; Xu, Y.; Zheng, Y. Distribution and Evolution of Supraglacial Lakes in Greenland during the 2016–2018 Melt Seasons. *Remote Sens.* **2022**, *14*, 55. [CrossRef]
19. Yang, K.; Li, M.C.; Liu, Y.X. Remote Sensing Study of Meltwater Storage, Transport and Release from the Greenland Ice Sheet. Ph.D. Thesis, Nanjing University, Nanjing, China, 2014.
20. Zhu, D.; Zhou, C.; Zhu, Y.; Peng, B. Evolution of supraglacial lakes on Sermeq Avannarleq glacier, Greenland using Google Earth Engine. *J. Hydrol. Reg. Stud.* **2022**, *44*, 101246. [CrossRef]
21. Qian, L.; Che, W.; Tong, Z.; Wei, C.; Minghu, D. Assessment of Greenland surface melt algorithms based on DMSP and SMOS data. *Adv. Polar Sci.* **2023**, *34*, 177–189.
22. Kwok, R.; Nghiem, S.V.; Steffen, K.; Tsai, W.Y. Detection of snowmelt regions on the Greenland ice sheet using diurnal backscatter change. *J. Glaciol.* **2001**, *47*, 539–547. [CrossRef]
23. Anderson, M.R.; Mote, T.L. Variations in snowpack melt on the Greenland ice sheet based on passive-microwave measurements. *J. Glaciol.* **1995**, *41*, 51–60. [CrossRef]
24. Al Bitar, A.; Mialon, A.; Kerr, Y.H.; Cabot, F.; Richaume, P.; Jacquette, E.; Quesney, A.; Mahmoodi, A.; Tarot, S.; Parrens, M.; et al. The global SMOS Level 3 daily soil moisture and brightness temperature maps. *Earth Syst. Sci. Data* **2017**, *9*, 293–315. [CrossRef]
25. Kerr, Y.H.; Waldteufel, P.; Wigneron, J.P.; Martinuzzi, J.; Font, J.; Berger, M. Soil moisture retrieval from space: The Soil Moisture and Ocean Salinity (SMOS) mission. *IEEE Trans. Geosci. Remote Sens.* **2001**, *39*, 1729–1735. [CrossRef]
26. Liu, Y. Multi-source data fusion of Antarctic ice sheet freeze-thaw datasets (1999–2019). *J. Glob. Change Data* **2020**, *4*, 325–331. (In English and Chinese)
27. Steffen, C.; Box, J.; Abdalati, W. Greenland Climate Network: GC-Net. In *Glaciers, Ice Sheets and Volcanoes: A Tribute to Mark F. Meier*; CRREL 96-27 Special Report; Colbeck, S.C., Ed.; US Army Cold Regions Reattach and Engineering (CRREL): Hanover, NH, USA, 1996; pp. 98–103.
28. Fang, Z.X. Summer surface temperature changes in the Greenland ice sheet from 2000 to 2020 and their implications for material bal-ance. *Glacial Permafr.* **2022**, *44*, 872–884.
29. Hall, D.K.; Comiso, J.C.; DiGirolamo, N.E.; Shuman, C.A.; Box, J.E.; Koenig, L.S. Variability in the surface temperature and melt extent of the Greenland ice sheet from MODIS. *Geophys. Res. Lett.* **2013**, *40*, 2114–2120. [CrossRef]
30. Hall, D.K.; DiGirolamo, N.E. *Multilayer Greenland Ice Surface Temperature, Surface Albedo, and Water Vapor from MODIS, Version 1*; NASA: Washington, DC, USA, 2019.
31. Yu, X.; Wang, T.; Ding, M.; Wang, Y.; Sun, W.; Zhang, Q.; Huai, B. Assessment of MODIS Surface Temperature Products of Greenland Ice Sheet Using In-Situ Measurements. *Land* **2022**, *11*, 593. [CrossRef]
32. Ryan, J.; Smith, L.; Van As, D.; Cooley, S.; Cooper, M.; Pitcher, L.; Hubbard, A. Greenland Ice Sheet surface melt amplified by snowline migration and bare ice exposure. *Sci. Adv.* **2019**, *5*, eaav3738. [CrossRef] [PubMed]
33. Yang, K.; Smith, L.C. Supraglacial streams on the Greenland Ice Sheet delineated from combined spectral–shape information in high-resolution satellite imagery. *IEEE Geosci. Remote Sens. Lett.* **2012**, *10*, 801–805. [CrossRef]
34. Dozier, J. Spectral signature of alpine snow cover from the Landsat Thematic Mapper. *Remote Sens. Environ.* **1989**, *28*, 9–22. [CrossRef]
35. Hall, D.K.; Riggs, G.A.; Salomonson, V.V. Development of methods for mapping global snow cover using moderate resolution imaging spectroradiometer data. *Remote Sens. Environ.* **1995**, *54*, 127–140. [CrossRef]
36. Moussavi, M.; Pope, A.; Halberstadt, A.R.W.; Trusel, L.D.; Cioffi, L.; Abdalati, W. Antarctic supraglacial lake detection using Landsat 8 and Sentinel-2 imagery: Towards continental generation of lake volumes. *Remote Sens.* **2020**, *12*, 134. [CrossRef]
37. Gorelick, N.; Hancher, M.; Dixon, M.; Ilyushchenko, S.; Thau, D.; Moore, R. Google Earth Engine: Planetary-scale geospatial analysis for everyone. *Remote Sens. Environ.* **2017**, *202*, 18–27. [CrossRef]
38. Zheng, L.; Cheng, X.; Shang, X.; Chen, Z.; Liang, Q.; Wang, K. Greenland Ice Sheet Daily Surface Melt Flux Observed From Space. *Geophys. Res. Lett.* **2022**, *49*, e2021GL096690. [CrossRef]
39. Tedesco, M.; Fettweis, X. Unprecedented atmospheric conditions (1948–2019) drive the 2019 exceptional melting season over the Greenland ice sheet. *Cryosphere* **2020**, *14*, 1209–1223. [CrossRef]
40. Zheng, L.; Li, L.; Chen, Z.; He, Y.; Mo, L.; Chen, D.; Hu, Q.; Wang, L.; Liang, Q.; Cheng, X. Multi-sensor imaging of winter buried lakes in the Greenland Ice Sheet. *Remote Sens. Environ.* **2023**, *295*, 113688. [CrossRef]
41. Shang, X.; Cheng, X.; Zheng, L.; Liang, Q.; Chi, Z. Decadal Changes in Greenland Ice Sheet Firn Aquifers from Radar Scatterometer. *Remote Sens.* **2022**, *14*, 2134. [CrossRef]

42. Perovich, D.K.; Grenfell, T.C.; Light, B.; Hobbs, P.V. Seasonal evolution of the albedo of multiyear Arctic sea ice. *J. Geophys. Res. Ocean.* **2002**, *107*, SHE 20-1–SHE 20-13. [CrossRef]
43. Tschudi, M.A.; Curry, J.A.; Maslanik, J.A. Airborne observations of summertime surface features and their effect on surface albedo during FIRE/SHEBA. *J. Geophys. Res. Atmos.* **2001**, *106*, 15335–15344. [CrossRef]
44. Curry, J.A.; Schramm, J.L.; Ebert, E.E. Sea Ice-Albedo Climate Feedback Mechanism. *J. Clim.* **1995**, *8*, 240–247. [CrossRef]
45. Mätzler, C. *Thermal Microwave Radiation: Applications for Remote Sensing*; IET: London, UK, 2006; Volume 52.
46. Matzler, C.; Aebischer, H.; Schanda, E. Microwave dielectric properties of surface snow. *IEEE J. Ocean. Eng.* **1984**, *9*, 366–371. [CrossRef]
47. Matzler, C.; Schanda, E.; Hofer, R.; Good, W.; Rango, A. Microwave signatures of the natural snow cover at Weissfluhjoch. In Proceedings of the NASA Conference Publication, Hampton, VA, USA, 5–7 November 1980.
48. Braithwaite, R.J. Positive degree-day factors for ablation on the Greenland ice sheet studied by energy-balance modelling. *J. Glaciol.* **1995**, *41*, 153–160. [CrossRef]